Applied Physics Letters

Terahertz quantum cascade lasers based on quaternary AlInGaAs barriers

Cite as: Appl. Phys. Lett. **103**, 041103 (2013); https://doi.org/10.1063/1.4816352
Submitted: 03 May 2013 • Accepted: 05 July 2013 • Published Online: 22 July 2013

K. Ohtani, M. Beck, G. Scalari, et al.

View Online Export Citation CrossMark

ARTICLES YOU MAY BE INTERESTED IN

Scattering processes in terahertz InGaAs/InAlAs quantum cascade lasers
Applied Physics Letters **97**, 221114 (2010); https://doi.org/10.1063/1.3504251

Thermoelectrically cooled THz quantum cascade laser operating up to 210 K
Applied Physics Letters **115**, 010601 (2019); https://doi.org/10.1063/1.5110305

Band parameters for III–V compound semiconductors and their alloys
Journal of Applied Physics **89**, 5815 (2001); https://doi.org/10.1063/1.1368156

QBLOX

1 qubit

Shorten Setup Time
Auto-Calibration
More Qubits

Fully-integrated
Quantum Control Stacks
Ultrastable DC to 18.5 GHz
Synchronized <<1 ns
Ultralow noise

100s qubits

visit our website >

© 2013 AIP Publishing LLC.

Terahertz quantum cascade lasers based on quaternary AlInGaAs barriers

K. Ohtani, M. Beck, G. Scalari, and J. Faist
Institute for Quantum Electronics, ETH Zurich, Zurich 8093, Switzerland

(Received 3 May 2013; accepted 5 July 2013; published online 22 July 2013)

Terahertz quantum cascade lasers incorporating lattice-matched quaternary AlInGaAs barriers grown by molecular beam epitaxy on InP substrate are reported. Four quantum well active region devices exhibited lasing at 3.8 THz with threshold current densities as low as 74 A/cm^2 at 10 K. From optical characterization and a doping study of the active region, an upper state lifetime of 8 ps, as well as a long transport time across the active region of 68 ps and a ratio of free carrier loss to gain cross sections of 4.6%, is reported. A maximum operating temperature of 130 K was achieved for a device with a conduction band discontinuity of 0.14 eV. © *2013 AIP Publishing LLC*. [http://dx.doi.org/10.1063/1.4816352]

The $In_{0.53}Ga_{0.47}As/Al_{0.48}In_{0.52}As/InP$ is a powerful material system for the fabrication of mid-infrared quantum cascade lasers (QCLs).[1,2] Its large conduction band offset energy (ΔE_c) makes it possible to operate at a wide spectral range.[3,4] Additionally, the small effective mass (m^*) in the quantum wells (QWs) increases the dipole matrix element and decreases the non-radiative scattering rates, leading to large optical gain coefficient.[5] Furthermore, InP substrates enable a highly developed device fabrication technique and can be used as a low loss waveguide. As a consequence, QCLs exhibit high output power at room temperature[6] with low electrical power consumption[7] which is important for practical industrial applications.

However, in the terahertz (THz) region, the relatively strong coupling demanded by efficient carrier transport requires the growth of very thin $Al_{0.48}In_{0.52}As$ barriers due to the large conduction band offset $\Delta E_{c.} = 0.52$ eV (Ref. 8) between well and barrier materials. This situation makes the laser operation characteristics very sensitive to growth variation and accuracy and limit laser performance. To overcome this drawback, lattice matched $In_{0.53}Ga_{0.47}As/GaAs_{0.51}Sb_{0.49}$ THz QCLs in which the $Al_{0.48}In_{0.52}As$ barriers are replaced by $GaAs_{0.51}Sb_{0.49}$ have been recently proposed and demonstrated.[9] Since this material system features a smaller ΔE_c (=0.36 eV) together with a barrier effective mass m^* (=0.045m_0), thicker barriers can be used. Recently high performance lasers with maximum operation temperature (T_{max}) of 143 K have been reported[10] exceeding the performance of the $In_{0.53}Ga_{0.47}As/Al_{0.48}In_{0.52}As$ material system by 20 K.

An alternative approach is to use a quaternary alloy AlInGaAs as a barrier material. AlInGaAs[11,12] lattice matched to InP that combines the two lattice matched ternaries $In_{0.53}Ga_{0.47}As$ and $Al_{0.48}In_{0.52}As$ compounds expressed as $(Al_{0.48}In_{0.52}As)_z(In_{0.53}Ga_{0.47}As)_{1-z}$ ($0 < z < 1$). Direct band gap energy hence varies from 0.81 eV ($In_{0.53}Ga_{0.47}As$) to 1.51 eV ($Al_{0.48}In_{0.52}As$). Figure 1 shows the computed ΔE_c of $In_{0.53}Ga_{0.47}As/Al_xInGa_yAs$ QW and m^* of Al_xInGa_yAs as a function of Al composition (x). Here, the conduction to valence band offset ratio of 0.73:0.27 was assumed[13] and the following bowing parameters were used: 0.22 eV for direct bandgap and −0.016 m_0 for m^*.[14] As seen in Fig. 1, m^* of Al_xInGa_yAs remains smaller than the one of $Al_{0.48}In_{0.52}As$, while ΔE_c can be tuned from 0 to 0.52 eV, in particular, to around 0.14 eV where high performance THz QCLs have been obtained using the $GaAs/Al_{0.15}Ga_{0.85}As$ material system.[15–17]

Figure 2 shows the computed conduction band diagram of one period of the four QW active region (AR)[18] under an applied field of 6.5 kV/cm. The band structure was simulated by a self-consistent Schrödinger-Poisson equation solver. In this study, an Al composition of x = 28% in the AlInGaAs barrier was selected to obtain a $\Delta E_c = 0.255$ eV. The first three QWs constitute the active part of the AR where laser action occurs. A diagonal transition is used to increase the non-radiative lifetime of the laser upper state lifetime (labeled "5") and to decrease the non-resonant electron injection to the lower states (labeled "4" and "3"). The computed energy separation (E_{ij}), dipole matrix element (z_{ij}), and normalized oscillator strength (f'_{ij}) between the subband i and j are $E_{54} = 12.2$ meV, $z_{54} = 3.3$ nm ($f'_{54} = 0.16$) and $E_{53} = 15.1$ meV, $z_{53} = 2.8$ nm ($f'_{53} = 0.14$). The injector region consists of a wide single QW for electron extraction from the active layer by longitudinal optical (LO) phonon scattering. The energy spacing (E_{21}) between the excited state (labeled "2") and the ground state (labeled "1") in the

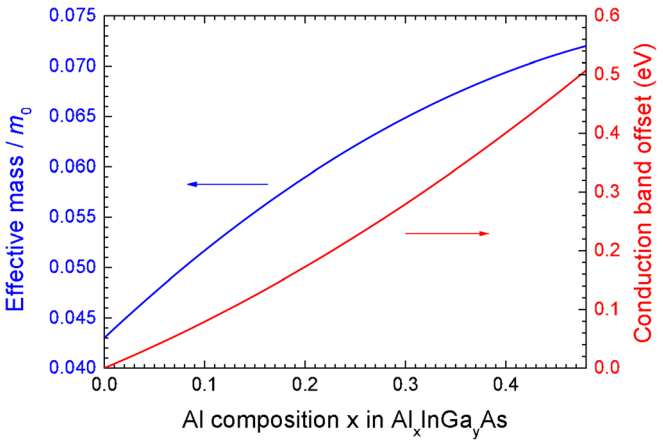

FIG. 1. Computed ΔE_c and m^* of quaternary Al_xInGa_yAs as a function of Al composition x (y = 0.48 − x). ΔE_c can be tuned in the wide range from 0 to 0.52 eV, whereas m^* remains small comparing to m^* of AlInAs. Here, we used the conduction and valence band offset ratio of 0.73:0.27.

 © 2013 AIP Publishing LLC

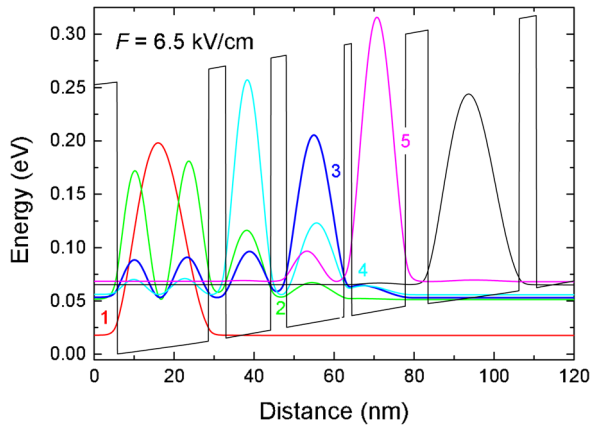

FIG. 2. Subband structure at an electric field of 6.5 kV/cm computed by self-consistent Schrödinger-Poisson equation solver. Starting from the wide QW, the layer thickness in nanometer is 22.8/**4.3**/11.3/**3.9**/14.3/**1.9**/13.5/**5.7**, where InGaAs layers are in roman font, AlInGaAs are in bold, and the silicon doped layer ($n_s = 5.06 \times 10^{10}\,\mathrm{cm}^{-2}$) is underlined.

wide QW is 33.7 meV, and its intersubband LO phonon scattering relaxation time is 0.33 ps. After relaxation, electrons are re-injected into the upper laser state of the adjacent AR by resonant tunneling. The computed coupling energy between injector and AR is 0.5 meV. The wide QW was uniformly doped with Si to $2.22 \times 10^{16}\,\mathrm{cm}^{-3}$ ($n_s = 5.06 \times 10^{10}\,\mathrm{cm}^{-2}$) to supply electrons.

The laser structure was grown on Fe-doped InP (001) substrate by solid-source MBE. The laser structure started with a 200 nm thick *n*-InGaAs bottom contact layer ($n = 3.0 \times 10^{18}\,\mathrm{cm}^{-3}$), followed by 150 periods of lattice matched InGaAs/AlInGaAs four QW AR. At the end, a 60 nm thick *n*-InGaAs top contact layer ($n = 1.0 \times 10^{19}\,\mathrm{cm}^{-3}$) was grown. X-ray diffraction spectra (not shown) exhibit many sharp satellite peaks reflecting a high structural quality. The calculated period thickness is in good agreement with the target one within 1% error. The MBE grown wafers were then processed into ridge laser structures with a double metal Au-Au waveguide. After removing the InP substrate, the bottom *n*-InGaAs contact layer was etched by 100 nm in order to decrease the waveguide losses. The processed wafers were cleaved into laser devices with ridge widths of 150 μm and cavity lengths of 1.4–2.5 mm.

Figure 3 shows current density (*J*)–voltage (*V*)–light (*L*) output characteristics of (a) pulsed and (b) continuous wave operation of a representative 1.44 mm long and 150 μm wide device. A feature in the *J*–*V* characteristic around $V = 2.8$ V is attributed to the onset of subband alignment between the ground state in the wide QW and the lower states of the laser transition. After pumping parasitic transport channel with small *J* ($\approx$24 A/cm^2), injection into the upper state starts for bias larger than $V > 6.5$ V, until a maximum current density is reached at ($J_{max} = 130$ A/cm^2). The threshold current density (J_{th}) in pulsed mode was 89 A/cm^2 at 10 K. The observed output peak power in pulsed mode (P_{max}) was 1 mW at 10 K and T_{max} was 50 K. In continuous wave mode, the devices showed similar laser characteristics as in pulsed mode. At 10 K, they delivered 0.8 mW output power with a slope efficiency of 8.2 mW/A and a T_{max} of 40 K. The low electrical power consumption of these devices provides almost the same T_{max} compared to T_{max} in the pulsed mode.

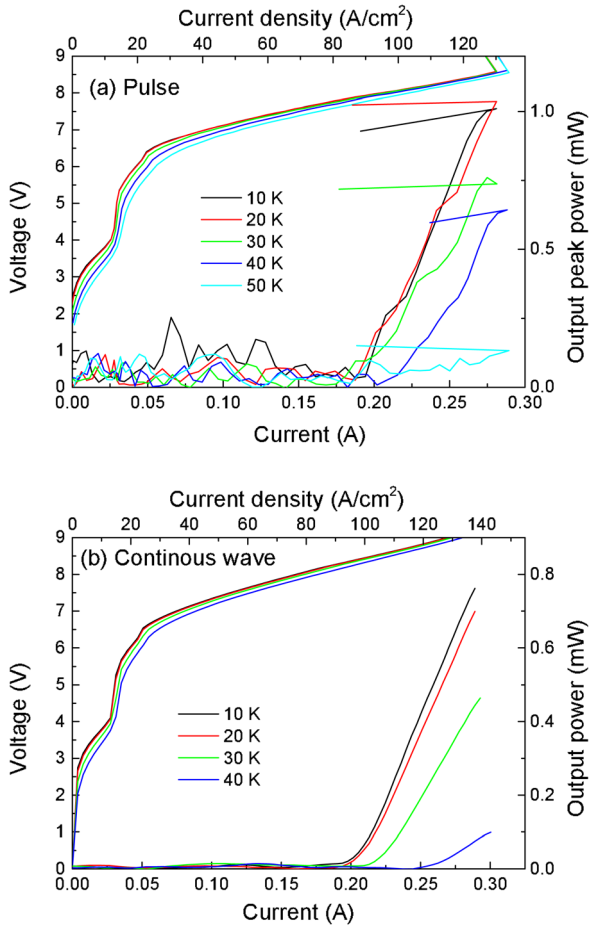

FIG. 3. (a) Pulsed current density (*J*)–voltage (*V*)–light (*L*) output characteristics of a 150 μm wide and 1.44 mm long ridge laser. Current pulses of 200 ns width at a duty cycle of 2% were used. The output power was recorded by a calibrated absolute terahertz power meter from Thomas Keating Ltd. (b) *L*–*J* and *J*–*V* characteristics measured in continuous wave mode.

Figure 4 shows an evolution of the laser emission spectra as a function of *J*. Here, the device with 2.5 mm long and 150 μm wide was used. The laser emission at 10 K had a multimode spectrum at the center frequency at 3.8 THz (15.8 meV). This is slightly larger than the computed value of E_{53} (15.1 meV) probably due to an underestimation of the conduction band offset energy. As seen in Fig. 4, the laser emission exhibits a blue shift with *J* due to the combined effects of cavity pulling and Stark shift originating from the diagonal nature of the laser transition. A frequency shift ($\partial\nu_L/\partial J$) via cavity pulling is related to a frequency shift of the gain curve ($\partial\nu_G/\partial J$) by Stark effect through the following equation:[19–21]

$$\frac{\partial \nu_L}{\partial J} = \frac{\hbar c G_M}{n_{eff}(2\gamma)} \frac{\partial \nu_G}{\partial J}, \tag{1}$$

where G_M is the modal gain, 2γ is the full width at half maximum of the gain curve, and n_{eff} is the effective refractive index. We hence could obtain G_M from the measured $\partial\nu_L/\partial J$ ($=6.7 \times 10^{-2}$ GHz/A·cm^{-2}) and $\partial\nu_G/\partial J$. Here, the frequency shift of the gain curve ($\partial\nu_G/\partial J = 1.7$ GHz/A·cm^{-2}) was estimated based on the envelope of the laser spectra shown in Fig. 4. By using the computed effective index (=3.7) and

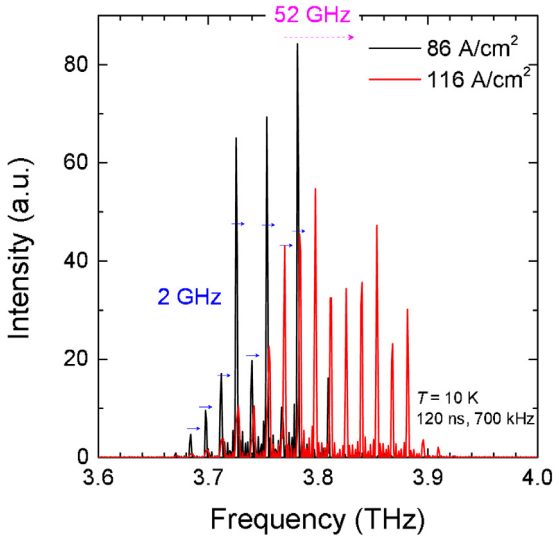

FIG. 4. Laser emission spectra from a 150 μm wide and 2.5 mm long ridge laser. Current pulses of 120 ns width at a repetition frequency of 700 kHz were used. The measured temperature was 10 K. The dotted line arrow indicates a frequency shift by Stark effect and the straight ones depict a shift via cavity pulling effect. The gain curve was shifted 52 GHz towards higher frequency. We also observed the shift (2 GHz) via cavity pulling.

assuming $2\gamma = 2.0\,\text{meV}$,[22] we obtain $G_M = 14\,\text{cm}^{-1}$ from Eq. (1). Moreover G_M is expressed as

$$G_M = g_c \frac{J_{th}\tau_{eff}}{e}, \tag{2}$$

where g_c is the gain cross section and τ_{eff} is the effective upper laser state lifetime.[19,23] The relation in Eq. (2) results in $\tau_{eff}^{(exp)} = 7.7$ ps using the computed g_c ($=4.4 \times 10^{-11}$ m) and measured J_{th} (67 A/cm^2 at 10 K for the 1.5 mm long device). For comparison, we calculated $\tau_{eff}^{(theo)}$ taking into account alloy disorder scattering, interface roughness scattering, and LO phonon scattering. Here, the average roughness height of 0.12 nm, the correlation length of 9 nm, and the alloy disorder potential of 0.6 eV for GaInAs and 1.4 eV for AlInAs[24] were used. From the computed τ_5 and the assumption of $\tau_{53} \ll \tau_3$, $\tau_{eff}^{(theo)} = 8.9$ ps was obtained, being consistent with the estimated $\tau_{eff}^{(exp)}$.

To investigate the limiting factor of laser operation, two other identical structures containing different doping concentration ($n_s = 3.65 \times 10^{10}\,\text{cm}^{-2}$ and $7.98 \times 10^{10}\,\text{cm}^{-2}$) in the wide QW were grown and their characteristics as a function of n_s were studied. Figure 5 shows J_{max} and J_{th} as a function of n_s. J_{max} was measured at 50 K, where the photon driven transport was not clearly detected. Results were summarized in Table I. J_{max} can be expressed as follows:[18,25,26]

$$J_{max} = en_s/\tau_{trans}, \tag{3}$$

where τ_{trans} is the global transit time of the electron across a period of the AR at the subband alignment. Therefore, the slope of the J_{max} versus n_s yields the inverse transport lifetime.[18,26] As expected, we observed a linear dependence on n_s with a small offset of J. By linear fitting of J_{max}, we obtained $\tau_{trans} = 68$ ps, which is about three times longer than the GaAs four QW THz QCLs ($=19$ ps).[18] The longer τ_{trans} is attributed to the thicker barrier of the present design.

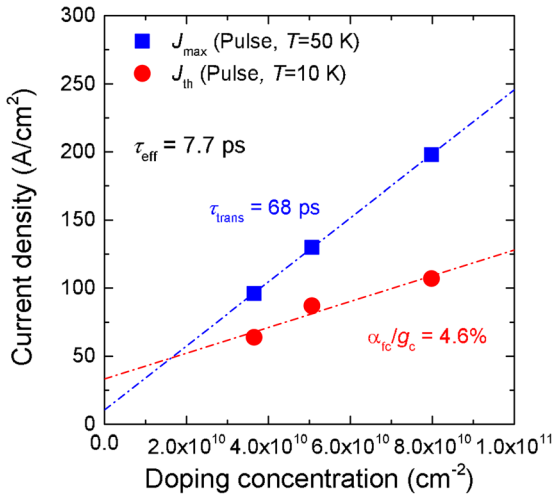

FIG. 5. Threshold current density (J_{th}) and maximum current density (J_{max}) as a function of doping concentration (n_s) in the wide QW. We measured J_{th} at 10 K and J_{max} at 50 K in pulsed mode. Transport time in one period ($\tau_{trans} = 68$ ps) and absorption cross section of active region ($\alpha_{fc} = (2.0 \pm 0.5) \times 10^{-12}$ m) were derived from Eqs. (3) and (4).

The small ratio of $\tau_{eff}^{(exp)}/\tau_{trans}$ (≈ 0.1) indicates that the electron transport time in the injection layer seems to be not fast enough to maintain a large electron population in the upper laser state. The small offset in J is interpreted as the result of a residual electron concentration of $n = (5.7 \pm 0.6) \times 10^{14}\,\text{cm}^{-3}$.

As a result of the strong undercoupling of our injector, we can safely assume that J_{th} of the device is determined by the waveguide losses and not by the voltage alignment condition.[27] In this model, J_{th} is written as[19,26]

$$J_{th} = \frac{e\alpha_{total}}{g_c\tau_{eff}} = \frac{e(\alpha_m + \alpha_{e-w})}{g_c\tau_{eff}} + \frac{e\alpha_{fc}}{g_c\tau_{eff}} n_s, \tag{4}$$

where α_{total} is the total loss, α_m is the mirror loss, $\alpha_{e\text{-}w}$ is the loss of the empty waveguide, and α_{fc} is the intersubband absorption cross section of AR.[19,26] The device with the lowest n_s ($=3.65 \times 10^{10}\,\text{cm}^{-2}$) exhibited the lowest J_{th} ($=74$ A/cm^2). As seen in Fig. 5, J_{th} does not extrapolate to zero as n_s approaches zero, confirming our assumption that J_{th} is determined by the waveguide losses as Eq. (4) is valid. The slope of J_{th} versus n_s hence gives α_{fc}/g_c and the offset of J_{th} yields $\alpha_m + \alpha_{e\text{-}w}$. Fitting our results yields for total empty cavity loss, $\alpha_m + \alpha_{e\text{-}w} = (7.2 \pm 2.9)\,\text{cm}^{-1}$ and for the ratio of the free carrier to gain cross section, $\alpha_{fc}/g_c = (4.6 \pm 1.1) \times 10^{-2}$, assuming that τ_{eff} is not dependent on n_s. The total empty cavity loss obtained here is in reasonable agreement with the waveguide loss reported previously.[28,29] In addition, $\alpha_{fc} = (2.0 \pm 0.5) \times 10^{-12}$ m was obtained, which leads to the AR waveguide loss ($=\alpha_{fc} \times n_s$) of $10.3 \pm 2.5\,\text{cm}^{-1}$ with $n_s = 5.06 \times 10^{10}\,\text{cm}^{-2}$. The total loss ($\alpha_{total}$ ($=\alpha_m + \alpha_{e\text{-}w} + \alpha_{fc} \times n_s$) $\approx 17.5\,\text{cm}^{-1}$) obtained

TABLE I. Summary of results on doping study. J_{th} and P_{max} were measured at 10 K, and J_{max} was measured at 50 K in pulsed mode.

n_s (cm^{-2})	J_{th} (A/cm^2)	J_{max} (A/cm^2)	P_{max} (mW)	T_{max} (K)
3.65×10^{10}	64	96	1.0	60
5.06×10^{10}	87	130	1.0	50
7.98×10^{10}	107	198	1.7	60

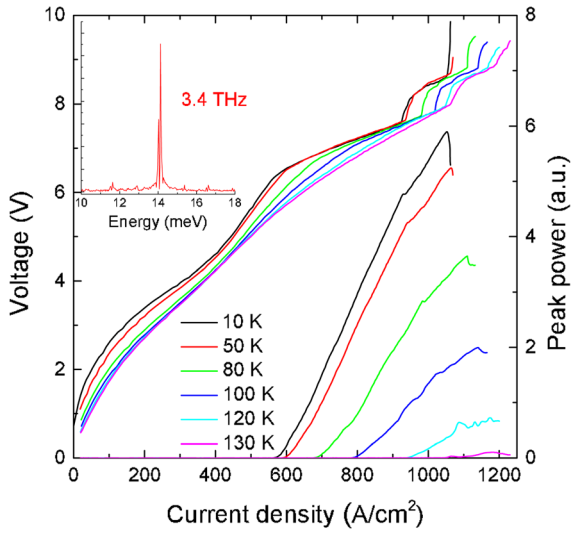

FIG. 6. Pulsed current density (J)–voltage (V)–light (L) output characteristics as a function of temperature of the sample with a lower ΔE_c (=0.14 eV). The ridge width was 150 μm wide and the cavity length was 1.5 mm long. The layer thickness in nanometer, starting from the wide QW, is 22.1/**4.1**/11.3/**3.6**/13.5/**2.0**/13.1/**5.2**, where InGaAs layers are in roman font, AlInGaAs are in bold, and the silicon doped layer ($n_s = 4.86 \times 10^{10}$ cm^{-2}) is underlined. The inset is a laser emission spectrum.

here is consistent with G_M (=14 cm^{-1}) from the analysis by cavity pulling. Also the waveguide loss is larger than the computed intersubband absorption tail of the wide QW ($\approx$2 cm^{-1}) if one neglects the electron heating; assuming the electron temperature is 100–120 K higher than the lattice temperature[30] yields a value close to the measured one.

Finally in order to decrease τ_{trans}, we fabricated THz QCLs with smaller ΔE_c. Here, an Al composition of 17% was chosen, providing ΔE_c (=0.14 eV). Figure 6 shows the temperature dependence of J-V-L curves of the device. We observed an improved laser performance of $P_{max} = 35$ mW at 10 K and $T_{max} = 130$ K, supporting the result obtained from the doping study. T_{max} exceeds that one (=122 K) of the ternary AlInAs barrier THz QCL by 8 K.[8]

In conclusion, we have proposed a quaternary AlInGaAs barrier material in InP THz QCLs and reported the first operation of GaInAs/AlInGaAs/InP THz QCL. The lasers emitted at 3.8 THz at 10 K. The observed J_{th} for the lowest n_s (=3.65 $\times$ 10^{10} cm^{-2}) was 74 A/cm^2. We have also derived τ_{eff} from gain analysis based on the cavity pulling being consistent with the computed one. From doping density dependent transport characteristics, a longer τ_{trans} is a source for limiting the present laser characteristics, which is confirmed by improved performance of THz QCL with the lower ΔE_c design.

The authors would like to thank Dr. R. Terazzi and Ms. J. Wolf for computing intersubband scattering time. M.B. dedicates this paper to Emanuel Mooser. This work was supported by ETH Zurich with the FIRST cleanroom facility and by the Swiss National Foundation under the NCCR project Quantum Photonics.

[1]J. Faist, F. Capasso, D. L. Sivco, C. Sirtori, A. L. Hutchinson, and A. Y. Cho, Science **264**, 553 (1994).
[2]M. Beck, D. Hofstetter, T. Aellen, J. Faist, U. Oesterle, M. Ilegens, E. Gini, and H. Melchior, Science **295**, 301 (2002).
[3]A. Bismuto, M. Beck, and J. Faist, Appl. Phys. Lett. **98**, 191104 (2011).
[4]N. Bandyopadhyay, Y. Bai, S. Tsao, S. Nida, S. Slivken, and M. Razeghi, Appl. Phys. Lett. **101**, 241110 (2012).
[5]E. Benveniste, A. Vasanelli, A. Delteil, J. Devenson, R. Teissier, A. Baranov, A. M. Andrews, G. Strasser, I. Sagnes, and C. Sirtori, Appl. Phys. Lett. **93**, 131108 (2008).
[6]Y. Bai, N. Bandyopadhyay, S. Tsao, S. Slivken, and M. Razeghi, Appl. Phys. Lett. **98**, 181102 (2011).
[7]B. Hinkov, A. Bismuto, Y. Bonetti, M. Beck, S. Blaser, and J. Faist, Electron. Lett. **48**, 646 (2012).
[8]M. Fischer, G. Scalari, K. Celebi, M. Amanti, Ch. Walther, M. Beck, and J. Faist, Appl. Phys. Lett. **97**, 221114 (2010).
[9]C. Deutsch, A. Benz, H. Detz, P. Klang, M. Nobile, A. M. Andrews, W. Schrenk, T. Kubis, P. Vogl, G. Strasser, and K. Unterrainer, Appl. Phys. Lett. **97**, 261110 (2010).
[10]C. Deutsch, M. Krall, M. Brandstetter, H. Detz, A. M. Andrews, P. Klang, W. Schrenk, G. Strasser, and K. Unterrainer, Appl. Phys. Lett. **101**, 211117 (2012).
[11]D. Olego, T. Y. Chang, E. Silberg, E. A. Caridi, and A. Pinczuk, Appl. Phys. Lett. **41**, 476 (1982).
[12]K. Alavi, H. Temkin, W. R. Wagner, and A. Y. Cho, Appl. Phys. Lett. **42**, 254 (1983).
[13]Y. Sugiyama, T. Inata, T. Fujii, Y. Nakata, S. Muto, and S. Hiyamizu, Jpn. J. Appl. Phys., Part 2 **25**, L648 (1986).
[14]I. Vurgaftman, J. R. Meyer, and L. R. Ram-Mohan, J. Appl. Phys. **89**, 5815 (2001).
[15]R. Köhler, A. Tredicucci, F. Beltram, H. E. Beere, E. H. Linfield, A. G. Davies, D. A. Ritchie, R. C. Iotti, and F. Capasso, Nature **417**, 156 (2002).
[16]S. Fathololoumi, E. Dupont, C. W. I. Chan, Z. R. Wasilewski, S. R. Laframboise, D. Ban, A. Mátyás, C. Jirauschek, Q. Hu, and H. C. Liu, Opt. Express **20**, 3866 (2012).
[17]B. S. Williams, Nature Photon. **1**, 517 (2007).
[18]M. Amanti, G. Scalari, R. Terazzi, M. Fischer, M. Beck, J. Faist, A. Rudra, P. Gallo, and E. Kapon, New J. Phys. **11**, 125022 (2009).
[19]J. Faist, *Quantum Cascade Lasers* (Oxford University Press, Oxford), Chap. 10, pp. 202.
[20]A. Yariv, *Quantum Electronics* (John Willy and Sons, New York), Chap. 9, pp. 187.
[21]G. Fasching, V. Tamošiūnas, A. Benz, A. M. Andrews, K. Unterrainer, R. Zobl, T. Roch, W. Schrenk, and G. Strasser, IEEE J. Quantum Electron. **43**, 687 (2007).
[22]M. Fischer, G. Scalari, C. Walther, and J. Faist, J. Cryst. Growth **311**, 1939 (2009).
[23]J. Faist, Appl. Phys. Lett. **90**, 253512 (2007).
[24]A. Vasanelli, A. Leuliet, C. Sirtori, A. Wade, G. Fedorov, D. Smirnov, G. Bastard, B. Vinter, M. Giovannini, and J. Faist, Appl. Phys. Lett. **89**, 172120 (2006).
[25]C. Sirtori, F. Capasso, J. Faist, A. Hutchinson, D. Sivco, and A. Cho, IEEE J. Quantum Electron. **34**, 1722 (1998).
[26]L. Ajili, G. Scalari, M. Giovannini, N. Hoyler, and J. Faist, J. Appl. Phys. **100**, 043102 (2006).
[27]A. Benz, G. Fasching, A. M. Andrews, M. Martl, K. Unterrainer, T. Roch, W. Schrenk, S. Golka, and G. Strasser, Appl. Phys. Lett. **90**, 101107 (2007).
[28]D. Dietze, J. Darmo, and K. Unterrainer, IEEE J. Quantum Electron. **46**, 618 (2010).
[29]M. Martl, J. Darmo, C. Deutsch, M. Brandstetter, A. M. Andrews, P. Klang, G. Strasser, and K. Unterrainer, Opt. Express **19**, 733 (2011).
[30]M. S. Vitiello, G. Scamarcio, V. Spagnolo, B. S. Williams, S. Kumar, Q. Hu, and J. L. Reno, Appl. Phys. Lett. **86**, 111115 (2005).